Front. Energy 2019, 13(2): 251–268
https://doi.org/10.1007/s11708-019-0625-z

REVIEW ARTICLE

Soheil RASHIDI*, Akshay CARINGULA*, Andy NGUYEN, Ijeoma OBI, Chioma OBI, Wei WEI

Recent progress in MoS_2 for solar energy conversion applications

Abstract In an era of graphene-based nanomaterials as the most widely studied two-dimensional (2D) materials for enhanced performance of devices and systems in solar energy conversion applications, molybdenum disulfide (MoS_2) stands out as a promising alternative 2D material with excellent properties. This review first examined various methods for MoS_2 synthesis. It, then, summarized the unique structure and properties of MoS_2 nanosheets. Finally, it presented the latest advances in the use of MoS_2 nanosheets for important solar energy applications, including solar thermal water purification, photocatalytic process, and photoelectrocatalytic process.

Keywords 2D nanomaterial, molybdenum disulfide, solar energy conversion, solar thermal conversion, photocatalytst, photoelectrocatalyst

1 Introduction

The discovery of graphene and its fascinating properties has stimulated serious research on other materials which have interesting properties when it comes to a two dimensional (2D) structure in comparison with their bulk materials [1–5]. Two dimensional transition metal dichalogenides (TMDs) is one of these group of materials which consists of the transition metal (M) and chalcogen (X) with the MX_2 formula [6–9]. MoS_2 is known as one of the very common transition metal dichalcogenides (TMDs) [6,7,10–13], which have the weakly interacting layered character of graphite and providing novel properties when it has a two dimensional structure [1,14]. The 2D layered structure MoS_2 could be found in enormous quantities in nature [8,9]. In the MoS_2 structure, two S atomic layers are attached to the Mo atomic layer by covalent bonds and make a sandwich structure with a thickness of 6–7 Å while the weak van der Waals bonds keep the two adjacent MoS_2 layers together [9,15–17]. There are a vast variety of applications for MoS_2, such as advanced energy storage and conversion [18], electrochemical catalysis [19,20], and sensing [21–23] due to its unique properties of the anisotropy. The structure of MoS_2 plays a very important role in the electrical conductivity of this material [24–27]. The metal coordination of a single layer MoS_2 could be observed as an octahedral or trigonal prismatic, as shown in Fig. 1 [28]. Hence, a number of these single layers could be made to produce various polymorphic structures which could be defined by the type of symmetry or the number of stacking layers in its unit cell (1, 2, or 3). Common polymorphs of MoS_2 could have tetragonal, hexagonal, and rhombohedral symmetries that are known as 1T, 2H and 3R structures, respectively. The 1T form shows a metallic behavior with a better conductivity in comparison to the semiconducting behavior of 2H and 3R forms. In other words, the 1T form has a better conductivity than the other two semiconducting forms. It has also been proved that the catalytic properties of these three forms are different, where the 1T phase has a better catalytic properties than 2H phase [29].

In this review, new approaches and various synthesis methods to synthesize MoS_2 is presented. This review is segmented into three main parts: preparation, which is described as top-bottom and bottom-top methods, such as liquid-based ultrasonic and mechanical exfoliations, chemical exfoliation via lithium ion intercalation, chemical vapor deposition, and hydrothermal-solvothermal approach; parameters affecting MoS_2 properties, which are discussed as structural strain, temperature, impurity doping, core-shell and structural defects; and the applica-

Received Jan. 8, 2019; accepted Mar. 6, 2019; online May 15, 2019

Soheil RASHIDI, Akshay CARINGULA, Andy NGUYEN, Ijeoma OBI, Chioma OBI, Wei WEI (✉)
Department of Mechanical Engineering, Wichita State University, Wichita KS 67260, USA
E-mail: wei.wei@wichita.edu

*These authors contributed equally to this work.

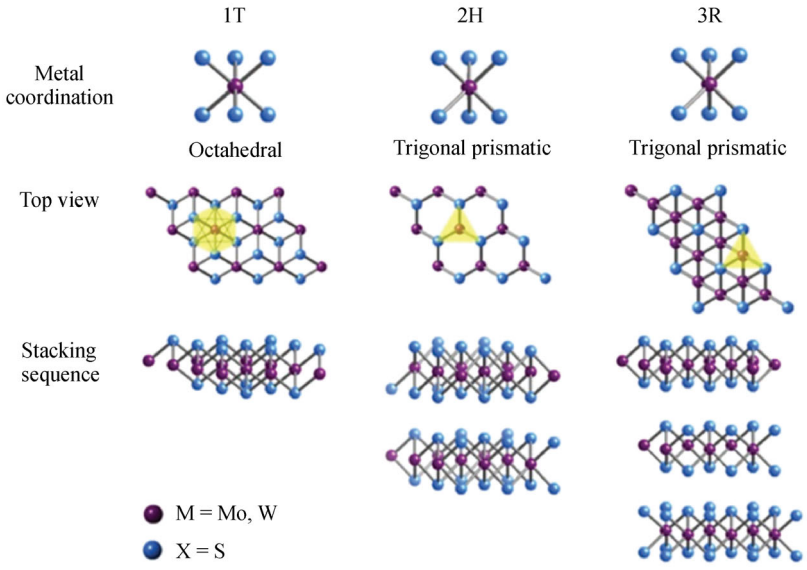

Fig. 1 Metal coordinate, top view, and stacking sequence of TMD structure (Reproduced from Ref. [28] with permission from the Royal Society of Chemistry)

tions of MoS_2, which is discussed in the area of solar thermal water purification, photocatalytic process and in photo electrocatalytic HER. It is arranged in a manner to facilitate the reader to grasp the in-depth idea about the technological developments in MoS_2 material for energy conversion applications and how MoS_2 stands out as a promising alternative 2D material for solar energy conversion.

2 Synthesis methods

Because of the attractive and important properties and the potential applications of MoS_2 nanosheets, various preparation methods have been demonstrated, such as mechanical exfoliation [30–34], electrochemical Li-intercalation and exfoliation [35,36], direct sonication in solvents [37,38], and chemical vapor deposition (CVD) [39,40]. The synthesis methods can be categorized into two general types: the top-down methods and the bottom-up methods. The top-down methods mechanically, ultrasonically, or chemically exfoliates bulk materials by overcoming the weak interlayer binding force, such as van der Waals, while the bottom-up methods assemble MoS_2 nanosheets using individual atoms.

2.1 Top-down methods

Mechanical exfoliation by Scotch tape can generate large, defect-limited, and electronic-grade MoS_2 nanosheets for fundamental studies [41,42]. However, this low yield, uncontrollable approach has limited usefulness in practical application, which usually requires a large quantity of nanomaterials with good quality. In contrast, liquid-based ultrasonic exfoliation can easily produce bulk dispersion of monolayer or few layer MoS_2 nanosheets or their mixtures [37,43]. Another advantage is that ultrasonic exfoliation does not induce any structural distortion and thus maintains the semiconducting 2H phase, unlike the phase conversion during the chemical exfoliation. However, the major limitation of ultrasonic exfoliation is that the raw product is mostly in a multilayer form.

To further increase the yield, chemical exfoliation has been used to produce MoS_2 monolayer via lithium ion intercalation [44]. In 2014, Voiry and coworkers functionalized TMD materials including MoS_2, WS_2, and $MoSe_2$, where the functionalization reaction is enabled by transferring electrons between the electron-rich metallic 1T phase and an organohalide reactant, contributing to functional groups that are covalently involved to the chalcogen atoms of the transition metal dichalcogenide [45]. Studies have shown that using butyllithium intercalation as the chemical exfoliation would result in crystal phases with dissimilar electronic properties in the nanosheets [46,47]. Take, for instance, the thermodynamically stable 2H phase in the trigonal prismatic MoS_2, where the butyllithium intercalation contributes to partial transformation of the crystal structure from the 2H phase to the octahedral 1T metallic phase caused by the electron transferring from the butyl group to the MoS_2 sheets, as shown in Figs. 2(a) and 2(b) [44,46,48].

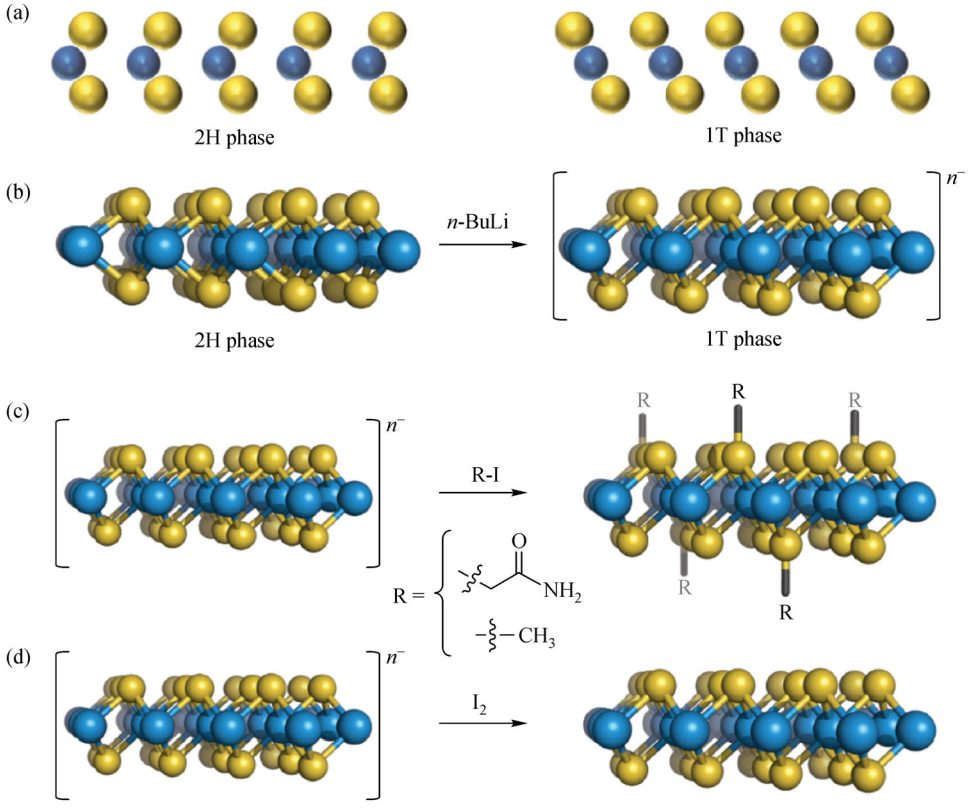

Fig. 2 Schematic of functionalization scheme

(a) Side view of the 2H and 1T phases; (b) 2H phase of TMDs converted to the 1T phase via lithiation using butyllithium (BuLi), and 1T phase negatively charged (*n*– indicates the excess charges carried by the exfoliated 1T-phase nanosheets.); (c) nanosheets functionalized by using 2-iodoacetamide or iodomethane (R-I) solution; (d) charge on the nanosheets also being quenched by reacting with iodine, with no covalent functionalization (Reproduced from Ref. [45] with permission from Springer Nature)

2.2 Bottom-up methods

MoS_2 nanosheets can also be produced by first decomposing Mo- and S-containing precursors and then assembling Mo and S atoms, such as chemical vapor deposition (CVD). CVD is a widely used technique for growing 2D nanomaterials in a controllable manner [40,49–52]. It can be classified into three options: thermolysis of precursors containing Mo and S atoms; vaporization and decomposition of Mo and S precursors and subsequent formation of MoS_2 layers on a growth substrates; and direct sulfurization of Mo-based films, such as Mo metal or MoO_3. Another widely explored bottom-up method is to use a hydrothermal-solvothermal reaction, which occurs in a sealed autoclave at high temperature and pressure [53–59]. This method usually produces hybrid 1T/2H phase in the as-prepared MoS_2 nanosheets, while pure 2H-MoS_2 can be obtained by post-annealing. Besides its simplicity and wide applicability, the hydrothermal-solvothermal approach is very attractive owing to its facile hybridization with other functional nanomaterials [60].

3 Parameters affecting MoS_2 properties

MoS_2 is a semiconductor with an indirect band gap and consists of S-Mo-S sheets that are held together by van der Waals interactions through a hexagonal structure [61]. However, the single layer MoS_2 has a direct gap with a band-gap energy of about 1.9 eV [42,62,63], hence it has become an exciting candidate for electronic, optoelectronic, and photovoltaic applications. In this review, the description of different parameters for tuning MoS_2 properties and various applications are mainly focused on. There are several parameters that affect the band gap and electrical properties of MoS_2.

3.1 Structural and strain effects

In 2012, Scalise et al. studied the electronic and vibrational properties of 2D honeycomb structures of MoS_2 by applying tensile and compressive biaxial strains to tune the in-plane XY orbital interactions, and therefore, increased the interlayer atomic distance [61]. They

observed that by increasing the level of applied strain, the shrinkage of energy band gap occurred. In other words, both the bottom of the valence band and the top of the conduction band would cross the fermi level and it is predictable to detect a transition limit of the system from semiconducting to metallic, while the strain range is about 8%–10%. There is not any significant difference observed in the case of Mo-S bond lengths and S-S distances with respect to the bulk structure for the multilayer MoS_2 structures with 1, 2 and 3 S-Mo-S. The nature of the gap and the electronic properties of layered MoS_2 could be affected by the variations in the charge interactions along the *Z*-direction (out-of-plane). They reported that the monolayer MoS_2 was tuned to an indirect gap semiconductor, even by applying less than 1% of tensile strain.

In 2014, Ebnonnasir et al. found out the band gap of MoS_2 could be affected by changing the orientation of graphene in MoS_2 heterostructures, and outlined the physical basis of this outcome to the highly sensitive dependence of the band gap value on the thickness of the MoS_2 layer [64]. The band structure would be changed due to any fluctuations through the band length that can happen by interfacial electronic transfer owing to applied changes in registry between graphene and MoS_2. They also showed that graphene-MoS_2 hetero-structures are delightfully appropriate for photovoltaic devices, in which the MoS_2 could form the exciton pair that would be collected at graphene layers situated on either side of the MoS_2 layer.

A number of other studies were conducted to investigate the effect of structure and strain on the band gap of TMDs [65–67]. Peelares et al. used the first-principles hybrid density functional theory to examine the electronic structure of MoS_2 and explore strain effects corresponding to experimentally accessible uniaxial and biaxial stress conditions [65]. The band structure could affect the tensile uniaxial strain, hence the transition from the bulk to the monolayer band structure can be monitored. Moreover, Shi et al. reported that WS_2 possessed the lightest effective mass at the same strain value compared to Mo(S,Se) and W (S,Se) monolayers [68].

3.2 Temperature effects

The crossover of band gap from direct to indirect band gap could occur by changing the temperature as well as structural and strain effects. In 2012, Tongay et al. explored the thermally driven crossover from indirect to direct band gap in two dimensional semiconductors by comparing $MoSe_2$ and MoS_2 [69]. In a few layer $MoSe_2$ that has a good thermal stability and a direct band gap of 1.55 eV, the indirect band gap and direct band gap are nearly degenerate, despite of the well-explored MoS_2. That is to say increasing the temperature contributes to the interlayer thermal expansion and reducing the coupling between the neighboring layers which results in the fact that the system would be driven toward the quasi-2D limit. In contrast, not only MoS_2 has a higher band gap than $MoSe_2$, but also the direct and indirect band gaps are well-separated in energy and consequently far from degeneration. As shown in Fig. 3(a), exfoliated few-layer flakes have the characteristic of A_{1g} (out-of-plane) and $E_{2g}{}^1$ (in-plane) Raman modes at two locations as 243.0 and 283.7 cm^{-1} for $MoSe_2$ and 408.7 and 383.7 cm^{-1} for MoS_2, respectively. The observed A_{1g} mode is at a higher frequency than the E_{2g} mode for $MoSe_2$. Additionally, the peak position of these Raman modes has a slight affiliation to the thickness of layers. Hence, for the single layer, the A_{1g} Raman mode relaxes to 241.2 (406.1) cm^{-1} as the $E_{2g}{}^1$ mode strengthens to 287.3 (384.7) cm^{-1} for $MoSe_2$. The out-of-plane A_{1g} mode is expected to unstiffen owing to the decrease in the restoring forces ascending from the lack of interlayer coupling, when the interlayer coupling is lacking in the single layer limit. It is of great importance to mention that this model does not account for the strengthening of the in-plane $E_{2g}{}^1$ mode. More captivatingly, the intensity ratio between the A_{1g} and $E_{2g}{}^1$ modes ($I_{A1g}/I_{E2g}{}^1$) increases from 4.9 for few-layer (~10 layers) to 23.1 for the single-layer $MoSe_2$, while the ratio remains nearly a constant (~1.2) in the MoS_2 case. In addition, the bulk $MoSe_2$ has an indirect band gap with a value of 1.1 eV [70], and therefore the band gap PL is anticipated to be relatively weak. However, the few layer $MoSe_2$ flakes display ongoing improvement in PL greatness at around 1.5 – 1.6 eV, and the PL peak intensity reaches its maximum value for a single-layer $MoSe_2$ as presented in Fig. 3(b). The temperature reliance of PL dignified on single- and few-layer samples of $MoSe_2$ and MoS_2 is displayed in Figs. 3(c)–3(f). The rate of the indirect-to-direct band gap crossover varies considerably between MoS_2 and $MoSe_2$. Even though single layer $MoSe_2$ is a direct band gap semiconductor (1.34 eV), the indirect band gap value (1.50 eV) lies near the direct band gap. This dissimilarity value of 0.16 eV is much slighter than the difference of 0.35 eV between the direct (1.54 eV) and indirect (1.89 eV) band gap for the single-layer MoS_2. By increasing the number of layers, the quantum confinement in the perpendicular direction is undisturbed, and consequently the indirect band gap tends to be reduced, while the direct band gap value remains largely unchanged, owing to the heavier effective mass associated with the K symmetry point.

3.3 Impurity doping

By comparing the bulk semiconductors with nanocrystals, the latter have a various and increasing range of factors that can control the electronic band gap of these materials as can be observed in Fig. 4, including size, shape, and composition. Quantum confinement can move the band gap of most semiconductors by over 1 eV, giving a huge range of continuous tunability through the size and shape for a single material composition [71]. The use of quantum confined structures permits the independent tuning of size

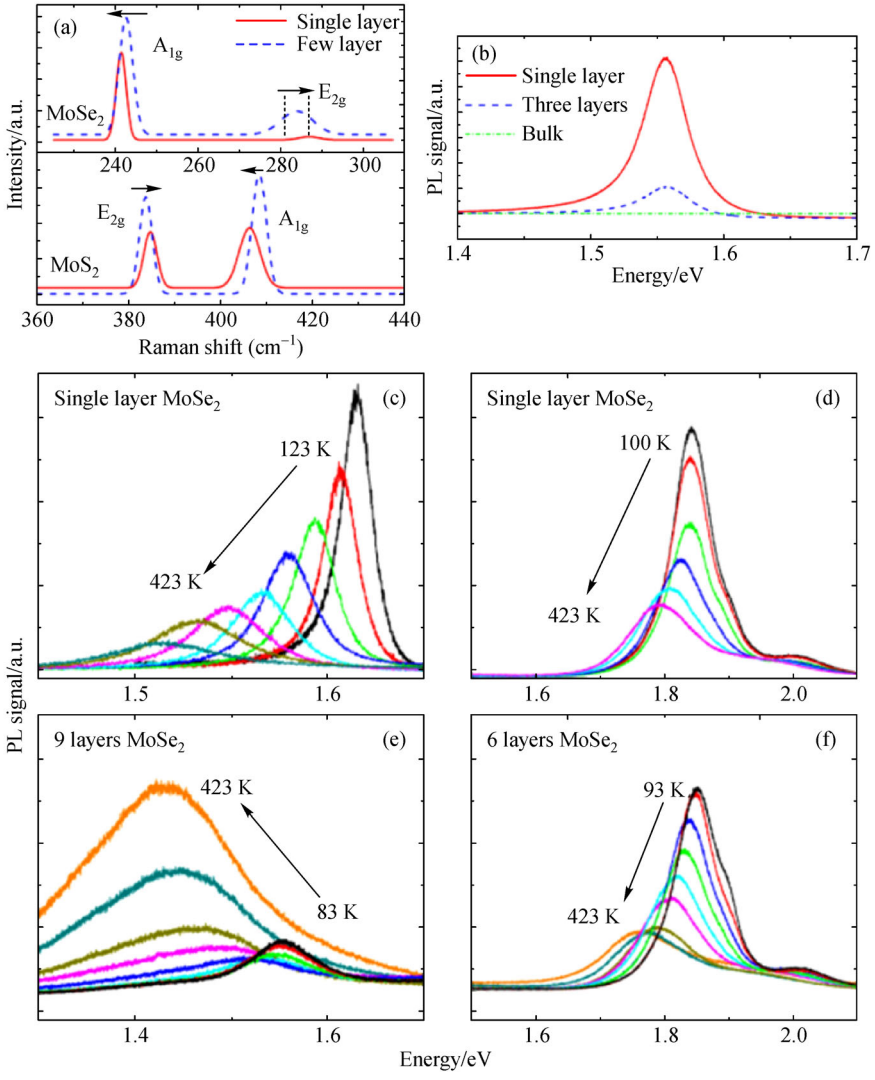

Fig. 3 Charaterization of $MoSe_2$ and MoS_2

(a) Raman spectrum of single (solid red line) and more than 10 layers (dashed blue line) MoX_2 (X = S, Se); (b) measured room-temperature photoluminescence on a single-layer (red), three-layer (blue dashed), and bulk (green dotted dashed) $MoSe_2$ (Here the measurement parameters including laser excitation intensity are the same. Temperature dependence of photoluminescence on (c–d) single-layer $MoSe_2$ and MoS_2 and (e-f) few-layer $MoSe_2$ and MoS_2. Here, the PL intensity ratio between the single-layer and few-layer MoX_2 typically reaches 50 − 500 (Reproduced from Ref. [69] with permission from American Chemical Society)

and band gap through the operation of homogeneously alloyed materials such as $CdSe_yTe_{1-y}$ and $Cd_xZn_{1-x}S$ [71]. Through a chemical alloying process by impurity doping, an intraband electronic energy level would be formed, which allows lower energy light emission to the ground state from the defect state. Doped nanocrystals have exciting properties for biolabeling and device applications, including large stokes shifts, paramagnetic properties, and improved lasing. However, due to the chemical contrasts between the dopants and their crystalline matrices, the creation of these doped nanocrystals is still a challenge.

Zhang et al. theoretically studied the influence of impurities on the electrical and optical properties of monolayer MoS_2 and concluded that the band gap would be dominated by donor impurities in 2017 [72]. They used the VB and VIIB transition metal atoms such as V, Nb, Ta, Mn, Tc, and Re and reported that the n-type or p-type doping could tune the Fermi level into the conduction band or the valence band, respectively. Therefore this leads to the degenerate semiconductor while the compensatory doped systems where the amount of valence electrons is not alerted keep on direct band gap ranging from 0.958 eV to 1.414 eV. By analyzing the densities of states, it has found that the LUMO orbitals of donor impurities play a critical part in band gap tuning. Owing to band gap reduction, doped MoS_2 has a minor threshold energy of

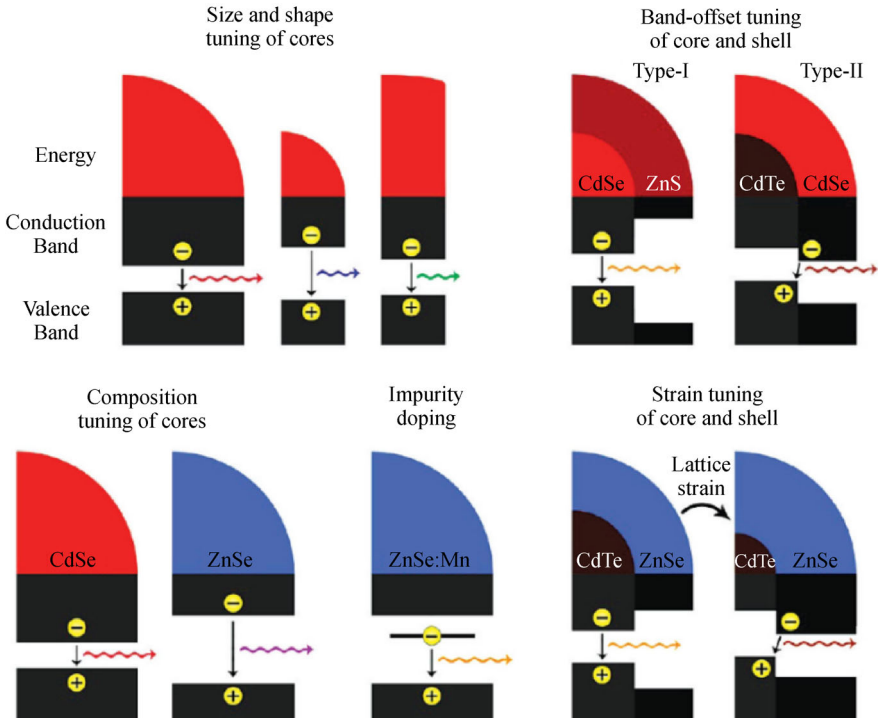

Fig. 4 Mechanisms of band gap engineering in semiconductor nanocrystals through size, shape, composition, impurity doping, heterostructure band offset, and lattice strain (Reproduced from Ref. [71] with permission from American Chemical Society)

photon absorption and an improved absorption in near infrared region. These outcomes deliver a noteworthy direction for the design of new 2D optoelectronic materials based on MoS_2 and other TMDs.

3.4 Core-shell (Type-II quantum dots)

In 2003, Bawendi et al. observed the separation of the electron and the hole between the core and shell materials through (core) shell semiconductor heterostructures, in which the conduction and valence bands of the core and shell material are staggered [73]. Li and coworkers reported that the flower-like $MoS_2/BiVO_4$ composite with heterojunction showed outstanding performance for photodegradation of methylene blue due to the staggered band alignment shaped between MoS_2 and $BiVO_4$ [74,75]. Based on these studies, the 2D-layered MoS_2 is found to have immense potential to be used for photocatalysis applications. It is of great importance to indicate that MoS_2 has some disadvantages, such as inadequate charge segregation and underprivileged charge mobility [76]. Both of them will lead to low photocatalytic behavior. Figure 5(a) is the UV absorption spectra of $BiVO_4$, MoS_2, and $BiVO_4$@MoS_2 where the bare MoS_2 nanosheets express noteworthy absorption both in the ultraviolet and visible regions. Meanwhile, the absorption wavelength for pure $BiVO_4$ lies around 500 nm and attributes to the intrinsic band gap absorption. By depositing MoS_2 nanosheets on the surface of $BiVO_4$, a better visible-light photocatalytic performance is observed for the composite in comparison with the pure $BiVO_4$. Moreover, the formula of $(\alpha h\nu)^n = A\,(h\nu - E_g)$ is being used to compute the band gap energy (E_g) of $BiVO_4$ and MoS_2, where h, ν, E_g, and A are the absorption coefficient, Planck's constant, light frequency, band gap, and a constant, respectively. In addition, the index n would be determined based on the electronic transition of the semiconductor. For instance n = 2 for direct-gap semiconductor and n = 0.5 for indirect-gap semiconductor would be considered. Therefore, the value of index n is equal to 2 for MoS_2 and $BiVO_4$. The band gap energy can be projected from the intercept of the tangent to the plot of $(\alpha h\nu)^2$ versus the radiation energy ($h\nu$), as can be seen in Figs. 5b–5f. They reported the band gap energy for $BiVO_4$ and nanosheet MoS_2 as 2.50 eV and 1.62 eV, respectively [77], while the bulk MoS_2 has shown a band gap energy of 1.23 eV [78], can be assigned to the strong quantum confinement effect of the thin nanosheets, which also makes the MoS_2 nanosheets an effective visible-light photocatalyst [79]. The values of band gap energy are reported as 2.19, 2.09 and 1.90 eV for $BiVO_4$@MoS_2 (2 wt%), $BiVO_4$@MoS_2 (5 wt%), and $BiVO_4$@MoS_2 (10 wt%), respectively. Since the photocatalytic property of the photocatalyst is contributed to its band structure, there is a simple approach to determine the band edge

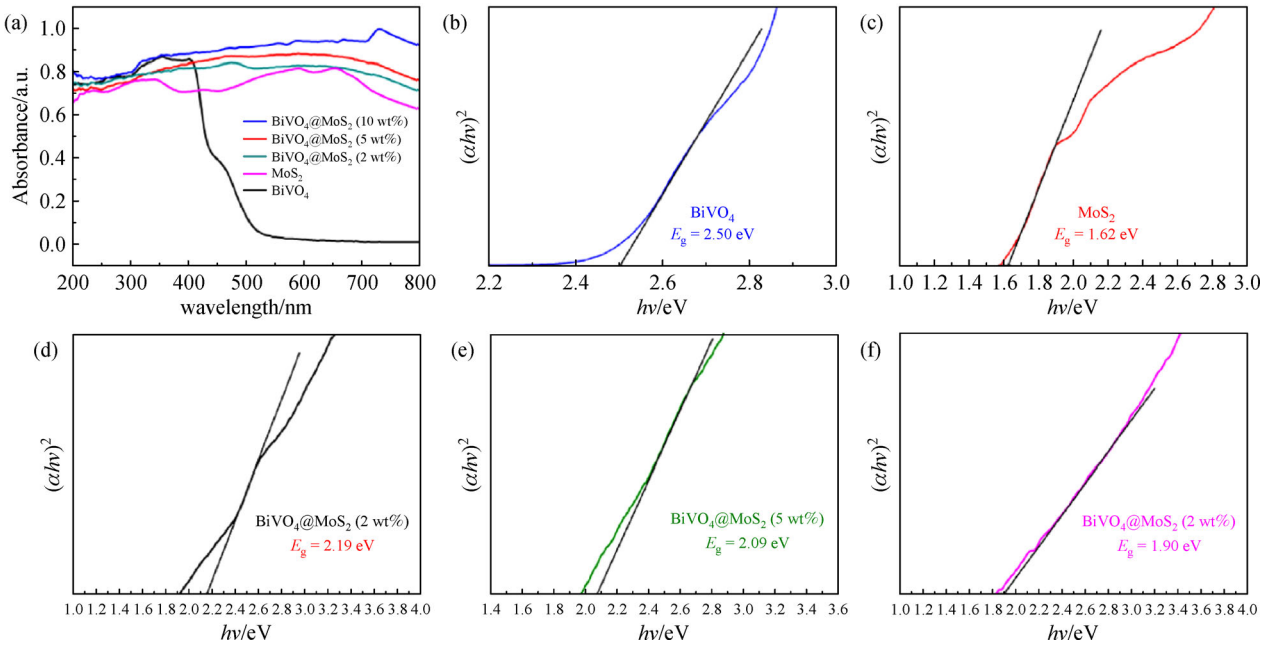

Fig. 5 (a) UV-vis absorption spectra of as-prepared $BiVO_4$, MoS_2 and $BiVO_4$@MoS_2; (b–f) the plot of $(\alpha h\nu)^2$ vs. energy $h\nu$ and band gap energy of the as-prepared samples (Reproduced from Ref. [80] with permission from Elsevier)

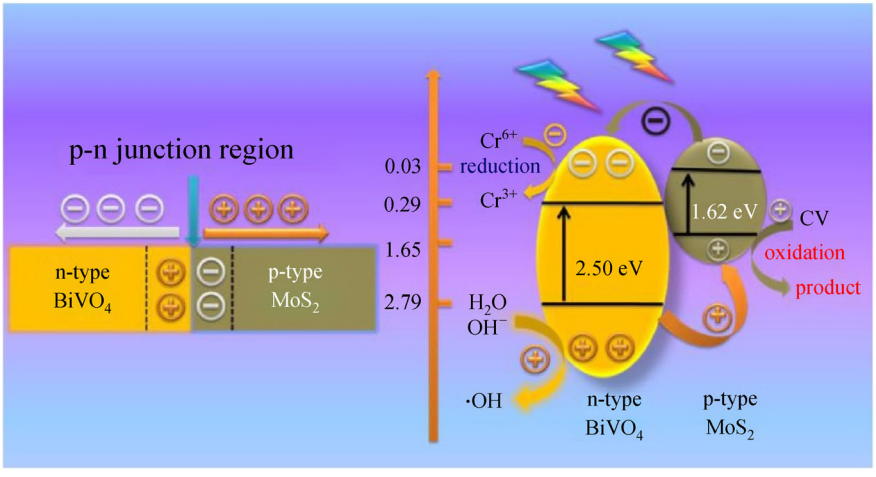

Fig. 6 p-n heterojunction photocatalyst formation model and the mechanism of photocatalysis of p-n heterojunction photocatalyst (Reproduced from Ref. [80] with permission from Elsevier)

positions of both the conduction band (E_{CB}). Besides, the valence band (E_{VB}) at the point of zero charge (pH_{ZPC}), can be calculated by $E_{CB} = X - E^e - 0.5E_g$ [80]. The X is the absolute electronegativity of the semiconductor, E^e is the energy of free electrons on the hydrogen scale (4.5 eV), E_g is the band gap, and the valence band edge (E_{VB}) can be determined by $E_{VB} = E_{CB} + E_g$. Therefore, the E_{CB} values of $BiVO_4$ and MoS_2 are determined to be 0.29 and 0.03 eV, respectively, where the E_{VB} values of $BiVO_4$ and MoS_2 are estimated to be 2.79 and 1.65 eV, respectively. Figure 6 demonstrates the photocatalysis mechanism of p-n heterojunction photocatalyst and the schematic drawing of the electron-hole separation process.

3.5 Structural defects

A number of studies have established that grain boundaries [81–83], the size of different constituents [84,85], and the interface with other monolayers [86] can greatly affect the electronic properties of two-dimensional semiconductors.

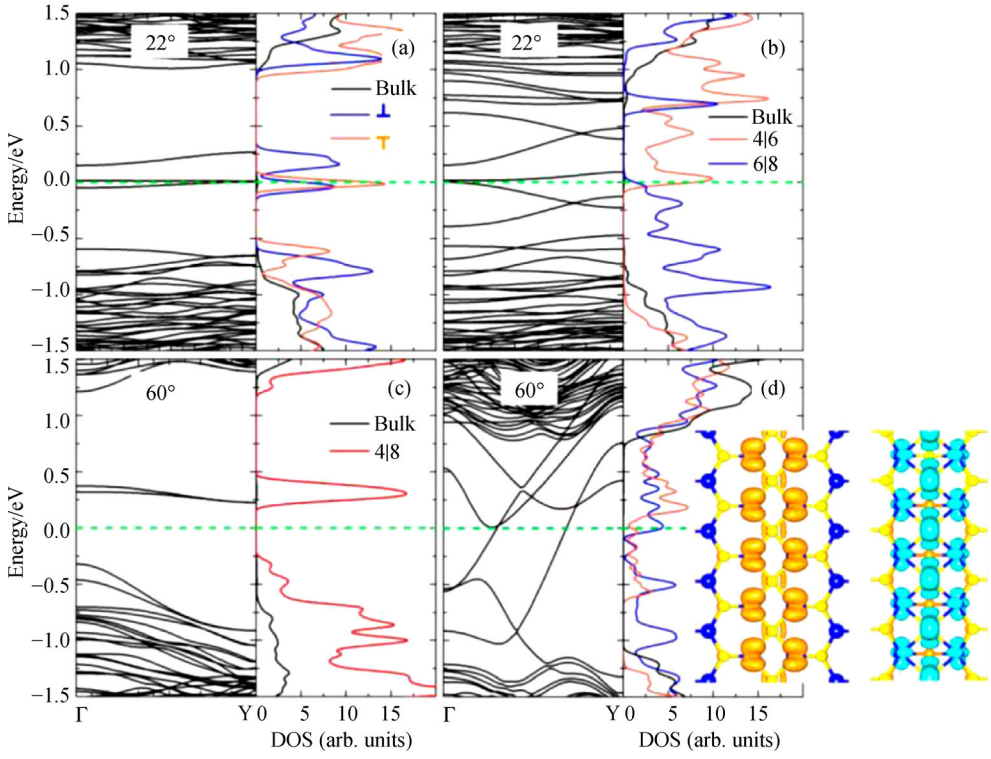

Fig. 7 Band structures and LDOS

(a) For 21.8° A-GB composed of ⊥ and T; (b) for 21.8° A-GB composed of 4|6 of 6|8; (c) for 60° Z-GB composed of 4|8; (d) for 60° A-GB composed of 4|6 and 6|8 (Green dashed lines indicate the Fermi level. Inset of (d) shows the partial charge density in the range of [–0.1, 0.1] eV. The DOS contribution of the bulk is projected to the Mo and S atoms far from the two parallel GBs (Reproduced from Ref. [83] with permission from American Chemical Society)

In 2012, Zou and coworkers theoretically considered predicting dislocations and grain boundaries in TMDs from the first principles [83]. As Fig. 7 demonstrates, the defects of extended grain boundaries (GB) take about significant changes to the electronic structures for MoS_2, where the direct band gap is calculated at K point as 1.8 eV for perfect MoS_2. Figures 8a–8d illustrate that the plots of local density of states (LDOS) and the presence of localized states could be observed with the energies intensely in the middle of the pristine MoS_2 gap which has been enhanced by the GB. The partial charge density distributions for these localized states have been computed and it is detected that they mainly initiate from the d orbitals of metal atoms in the Mo- and S-rich GBs, or from localized p states of S atoms in 6|8s. By reducing the carriers, these deep states may cut down the performance of devices based on polycrystalline MoS_2, A-GB's of other tilt angles. The local bands turn out to be dispersive for a greater tilt α where the cores are situated denser and relate with each other more tenaciously, and the discrete metallic behavior is emerged at $\alpha = 60°$ (from AC) GB. The states delocalized in one dimension associate with the metallic stripe bands overpassing the Fermi level. The inset of Fig. 7(d) shows the metallic behavior through the partial charge density during the LDOS contribution and proves that the wave functions are certainly corresponding to the GB and can be identified by scanning tunneling microscopy (STM). This study has shown that such metallic stripes could indeed introduce novel and valuable functionality brought by carefully engineered GB, in contrast to their more often detrimental role. Figure 9 shows the basic edge dislocations shaped by removal of shaded atoms from the lattice.

4 Applications of MoS_2

4.1 Solar thermal water purification

Due to the increase in global population and demand for clean fresh water, major developments for water treatment are taken into consideration. Solar steam generation based on photothermal effect has attracted great attention as a new water treatment technique because of the present of abundant and sustainable sunlight. Until now for efficient light absorption, carbon-based materials like graphene, graphene oxide and carbon nanotubes have been used for the treatment. The results indicate that by using the carbon-based material, the solar energy conversion efficiency is low, which needs to be rectified for better results. The

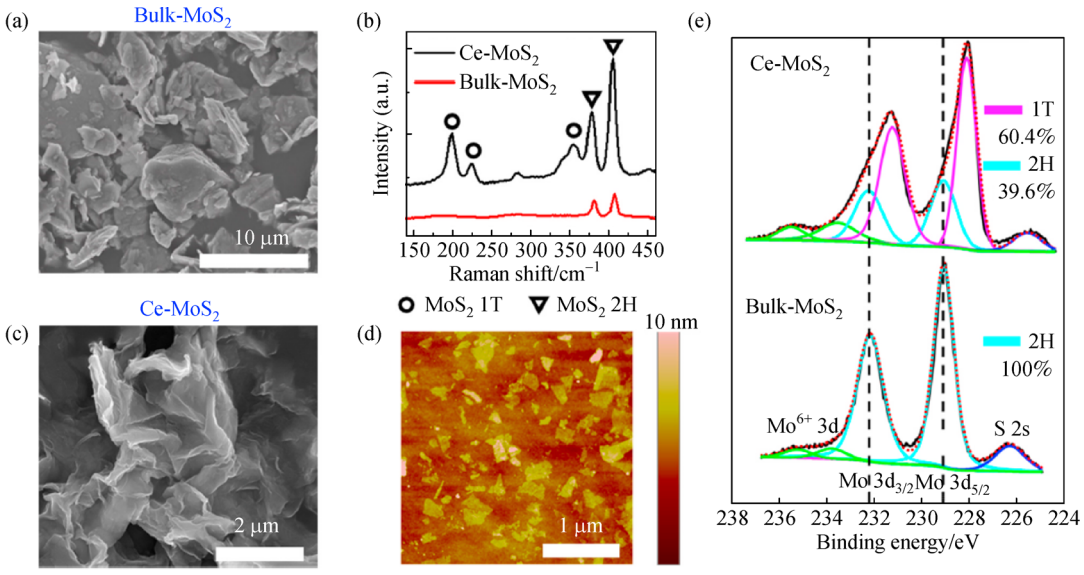

Fig. 8 Characterization of MoS_2

(a) SEM images of Bulk-MoS_2; (b) Raman spectra of ce-MoS_2 and bulk-MoS_2; (c) SEM images of ce-MoS_2; (d) AFM images of ce-MoS_2 nanosheets deposited on a silicon substrate; (e) XPS spectra of the ce-MoS_2 and bulk-MoS_2 [132] (Copyright Wiley-VCH. Reproduced with permission)

synthesis of these materials requires many steps and high temperature procedures by which the cost effectiveness issue comes into consideration as it is an important factor for solar thermal treatment. By considering the above factors, the need for cost effective, scalable and highly efficient photothermal materials is required. Chemically exfoliated MoS_2 is used for the generation of fresh water, as MoS_2 is highly efficient, scalable, and environmentally benign for solar evaporators. It was also reported that phase transition of MoS_2 from 2H phase which is a trigonal prismatic coordination to 1 T phase which is a octahedral coordination during the exfoliated process could enhance the light absorption of the ce-MoS_2 [60,87].

Jun et al. first investigated the earth-abundant and economical MoS_2 as a suitable material for solar steam generation [88]. Bulk MoS_2 particles showed multiple-stacked sheets with large lateral dimensions as shown in Fig. 8(a). The exfoliated MoS_2 nanosheets had an average thickness of 1.5 nm with lateral dimensions of 200–800 nm, as revealed by atomic force microscopy (AFM) images (Fig. 8(d)). X-ray photoelectron spectroscopy (XPS) was used to analyze the phase composition, as shown in Fig. 8(e). The spectrum of bulk MoS_2 exhibited only 2H peaks at 229.4 and 232.6 eV, suggesting that natural MoS_2 consists of only the 2H phase. In contrast, the peaks corresponding to ce-MoS_2 shifted to lower binding energies, and 1T phase peaks could be identified at 228.7 and 231.8 eV upon deconvoluting the spectrum using Gaussian-Lorentzian curve-fitting. During the Li intercalation process, the phase transition from 2H to 1T drastically increased the evaporation rates of chemically exfoliated (ce)-MoS_2/bacterial nanocellulose (BNC), because of the effective heat localization and good light absorption at the water/air interface. The cost effective, efficient steam generation of ce-MoS_2 nanosheets, along with their low cytotoxicity, promise their utility as a photothermal material for solar steam generation, water desalination and sterilization, and photothermal therapy.

4.2 Photocatalytic process

An effective photocatalyst relies on its band edge positions, which determines the redox potentials of photo-generated electrons and holes. In general, as the potential of conduction band (or valence band) becomes smaller (or larger), the photogenerated electrons (or holes) have a stronger reductive (or oxidative) capability [89]. The appropriate band structure makes MoS_2 nanosheets one of the most promising photocatalyst candidates.

Hydrogen has been considered as a clean energy resource that can be easily stored and used without producing any greenhouse gases. Since the emergence of photocatalytic water splitting in 1972 [90], hydrogen evolution reaction (HER) via photocatalysis has attracted enormous attention because it only requires water and solar energy. However, producing the conventional photocatalyst involves the utilization of noble metals or alloys, such as Pt, which hinders their large-scale application [91]. Thus, the development of competitive alternatives to noble metals is pursued. MoS_2 has recently been regarded as a promising candidate of noble-metal-free co-catalyst as it is an earth-abundant and visible light-responsive photocatalyst with unique physical and chemical properties [92,93]. Chang et al. systematically investigated the relationship

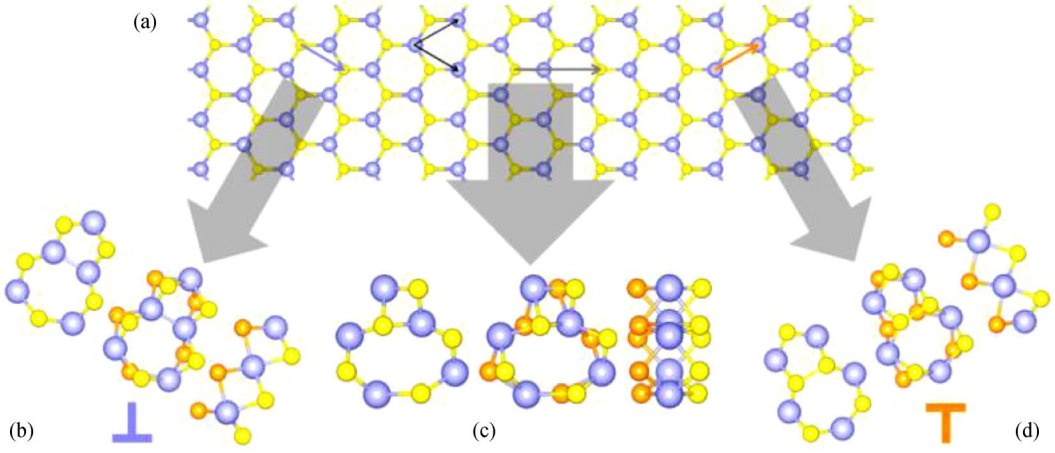

Fig. 9 Basic edge dislocations formed by removal of shaded atoms

(a) From the lattice; (b) with atomic structures of metal-polar ⊥; (c) a 4|8 in; (d) sulfur-polar ⊤ (Thin black arrows show the basis vectors, while the Burgers vectors are colored as blue (1, 0), orange (0, 1), and gray (1, 1). Each atomic structure is shown in front, isometric, and side (along the layer) views, with atoms colored blue (metal, M), yellow (front/top layer sulfur, S) and orange (back/bottom layer sulfur, S′) (Reproduced from Ref. [83] with permission from American Chemical Society).)

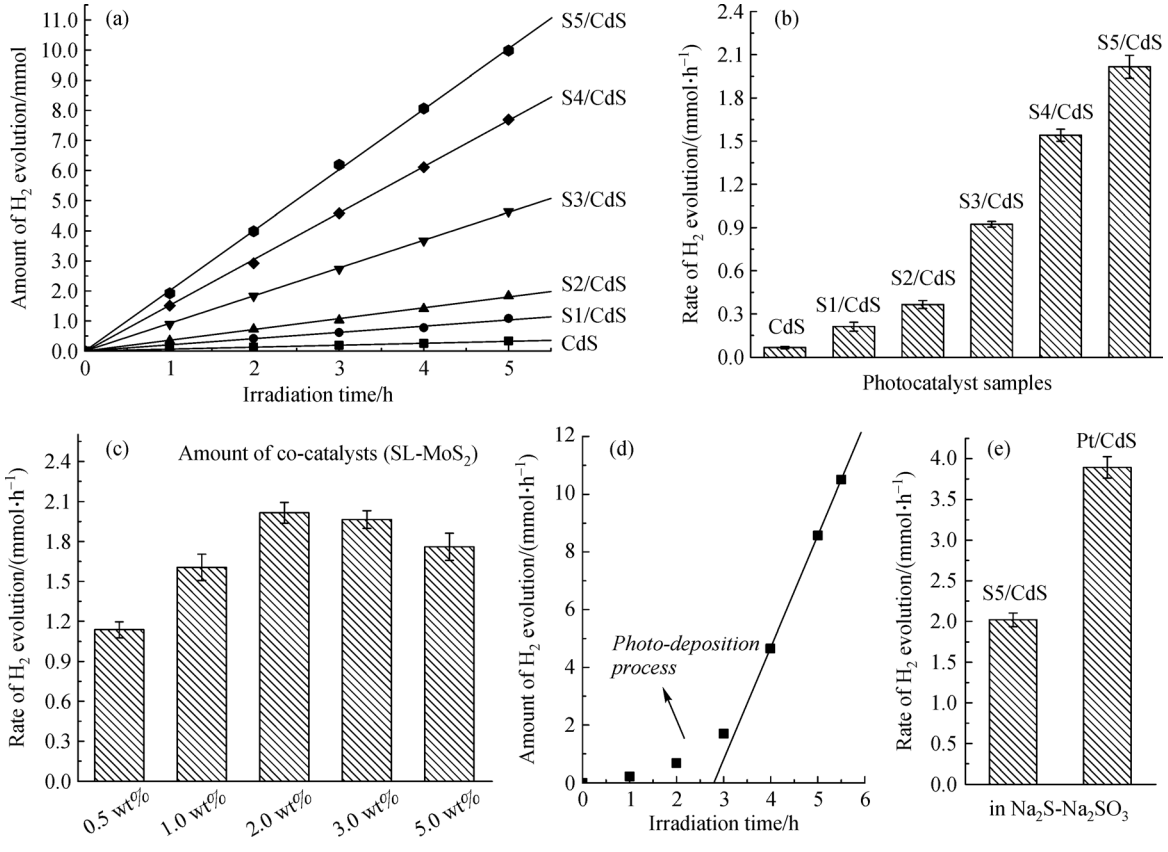

Fig. 10 Performance evaluation of catalysts

(a, b) Photocatalytic H_2 production activities of different samples in which the amount of cocatalyst is 2.0 wt%;(c) optimized content of SL-MoS_2 cocatalysts over CdS; (d) photocatalytic H_2 production activities of CdS loaded 0.65 wt% of Pt; (e) comparison of H_2 evolution activities of SL-MoS_2/CdS with Pt/CdS (Light source: 300-W Xe lamp with a L42 cut-off, $\lambda > 420$ nm. Reaction solution: 300 mL of 0.35 mol L^{-1} of Na_2S-Na_2SO_3 aqueous solution. Cat. 0.2 g [94].) (Copyright Wiley-VCH. Reproduced with permission)

between MoS_2 layer number and photocatalytic hydrogen generation activity [94]. MoS_2 loaded CdS (MoS_2/CdS) with MoS_2 layer numbers varying from 1 to 112 were prepared in their study. The corresponding hydrogen production activity in Na_2S-Na_2SO_3 and lactic acid solutions were explored, as shown in Fig. 10. It was demonstrated that the photocatalytic activity is increasing with decreasing MoS_2 layer number and highest H_2 production rate was achieved when the MoS_2/CdS had a single layer (SL) MoS_2. This layer-number-dependent photocatalytic activity is contributed to three major reasons. The first one is that the unsaturated S atoms of the exposed edge sites are the active sites of hydrogen generation. With the decrease of MoS_2 layer number, more active S atoms are exposed compared to the bulk material. The second one is that reducing the MoS_2 layer number is beneficial to the separation of charge carriers. It is easier for electrons to transport from CdS to SL MoS_2 than the bulk material. Finally, the conduction band minimum (CBM) of SL MoS_2 is not only more negative than H^+/H_2 potential but also negative versus the CBM of bulk form, thereby more electrons in the conduction band can reduce H^+ to H_2.

The metallic 1T-MoS_2 has a tremendous photo-induced catalytic activity because of the tunable band gap and the fact that both the edges and the basal plane of the 1T-MoS_2 are catalytically active. The metallic 1T- MoS_2 nanosheets can also act as an ideal support and co-catalyst for various composite catalyst which gives further enhancements in the performance in the presence of a photocatalyst. These characteristics make 1T-MoS_2 nanosheets and their composites a promising substitute to noble catalyst-based photocathodes for solar light-driven catalytic applications. Han et al. proposed that few layers MoS_2 coating on TiO_2 nanosheets (MST) will increase the photocatalytic activity for hydrogen production [95]. The report from the experimental and theoretical calculations stated that MST as a photocatalyst showed a significant low-charge recombination rate and excellent long-term durability. The authors also reported that there was a significant increase of 31.9% in photocatalytic activity for the hydrogen production when compared to TiO_2. Hsiao et al. developed a one-pot synthesis method for the preparation of 1T-MoS_2 for photocatalytic hydrogen evolution (HCS) [96]. He stated that the amount of hydrogen evolved over 1T-MoS_2@HCS reached 143 μmol in two hours which was 3.6 times higher when compared to that of 2H-MoS_2@HCS. Furthermore, 1T- MoS_2 could also be used as a counter electrode material for dye-sensitized solar cells (DSSCs), which had a higher conversion efficiency when compared to 2H- MoS_2@HCS counter electrode.

Over the past few years, MoS_2 has also been identified as efficient photocatalysts to degrade organic-pollutants in wastewater. MoS_2 is a nontoxic environment friendly material which has shown a good stability against photo corrosion and a good absorbent of the solar spectrum [97–100]. Since pure MoS_2 has a low photocatalytic performance, it has been combined with other semiconductor materials [101]. This combination allows a rapid charge separation due to different energy level forms of each semiconductor [102]. Several studies have been developing various combinations such as MoS_2/RGO composites [103], MoS_2 nanosheets supported by TiO_2/g-C_3N_4 photocatalysts [104], ZnO-MoS_2-RGO heterostructure [105], MoS_2/BiOBr microspheres [106], and flower like MoS_2/CdS heterostructures [107].

Extensive research has been conducted for the photocatalytic inactivation of microbial pollutant due to the superior inactivation ability of photocatalytic semiconductors compared with the conventional disinfection methods [108–110]. The mechanism of photocatalytic disinfection involves reactive oxygen species [110], which can trigger the breakdown of cell membranes and then promote the internalization of the semiconductor photocatalyst, ultimately leading to cell death [111,112]. Therefore, improving the separation of photogenerated electrons and holes is in favor of photocatalytic disinfection efficiency. Awasthi et al. attached flower-like ZnO on the surface of layered MoS_2 via the hydrothermal method [113]. An enhanced antibacterial activity was observed by using gram negative *E. coli* bacteria in comparison with pristine ZnO and MoS_2. It is not only attributed to the efficient separation rate of electron and hole pairs in the ZnO/MoS_2 nanocomposite, but also the increased surface area induced by the layered MoS_2. Liu et al. prepared a ternary photocatalyst (carbon nanotubes(CNTs)-MoS_2-Ag) and discovered its antibacterial activity against the Staphylococcus aureus and *Escherichia coli* [114]. It is reported that the antibacterial mechanism of this material not only includes the microorganism killing effect of Ag particles, but also relies on light absorption.

4.3 Photoelectrocatalytic HER

Utilization of semiconductor thin films as photoelectrode in photoelectrocatalytic water splitting application has been considered as a clean and reproducible energy [115,116]. The photoelectrocatalytic HER relies on the catalyst material having two properties: the material should be active for the electrocatalytic HER, and it should absorb sunlight, giving an electron hole pair with the right potential to drive the HER reaction. Recently, sizeable amount of highly active photocatalysts have been reported where they all possess one identical weakness in respective developments. That is, their wide band gaps have caused a major stumbling block in the refinement of their photocatalytic properties [117].

MoS_2 is a semiconductor with a direct band gap around 1.7 eV, indirect band gap at around 1.2 eV [118], and the band position slightly more positive than that for the HER [119]. This makes MoS_2 a promising candidate for use in a

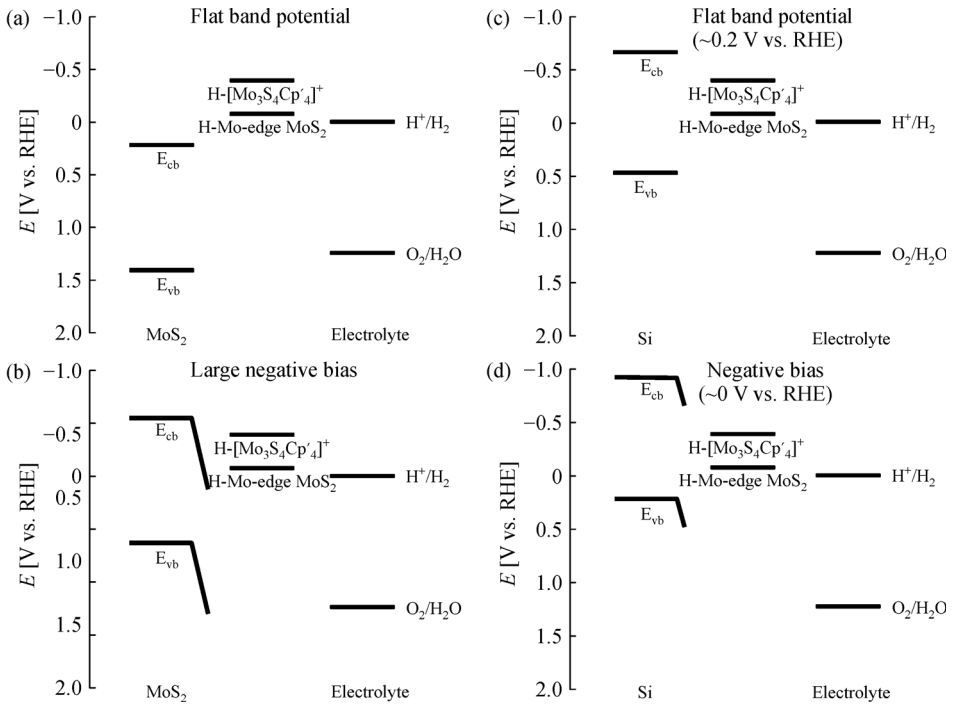

Fig. 11 Band gap position and redox levels for the HER for (a) MoS_2 at the flat band potential; (b) MoS_2 at large negative bias; (c) Si at flat band potential; and (d) Si at negative bias (From the figure it is seen that the HER does not occur spontaneously on bulk MoS_2, but requires additional quantum confinement, or high p-type donor concentrations. In (b) the MoS_2 is biased enough that the HER occurs, the exact potential cannot be defined. On Si the HER occur readily even at slightly positive bias vs. RHE, until the flat band potential (c) at more negative potentials the HER occurs even faster (d) (Reproduced from Ref. [121] with permission from Royal Society of Chemical)

tandem approach for the HER side if the conduction band could be pushed to slightly more genitive values (Fig. 11 (a)). This means that MoS_2 will not evolve hydrogen when illuminated [120] unless a negative bias (Fig. 11(b)) or quantum confinement is introduced [121]. The second way to utilize MoS_2 as a photoelectrocatalyst is to use the electrocatalytic HER activity together with a good photon absorber (exemplified for Si in Fig. 11(c)). In these systems, the distinct difference to pure MoS_2 is clearly seen, as in these systems the photon absorber may be freely chosen to provide the sufficient overpotential to drive the HER. A novel MoS_2 nanomaterial comprising a narrow-but-targeted direct band gap has been produced [121] and MoS_2 has proven to have an excellent electrocatalytic hydrogen evolution activity and active edge defect sites [122–124]. He et al. reported that 1T-MoS_2/TiO_2 nanotubes and 1T- MoS_2/Si-doped TiO_2 nanotubes had a high conductivity and an excellent catalytic activity for HER [125]. MoS_2 decoration provided high light absorbance property for these hybrids and the highly interface-induced effect between nanotubes and MoS_2. The results illustrated that the hybrids showed higher photocatalytic and photoelectrocatalytic activities than TiO_2. Li et al. reported that when 1T-MoS_2 were coupled with inorganic-lig and stabilized CdSe/ZnS quantum dots through the process of self-assembly approach, it could be used for various applications in solar to fuel conversions [126]. Under the optimum condition, hydrogen gas is produced at a rate of 155 μmol/h per mg. As a result of improved light harvesting, facilitated interfacial charge transfer and excellent proton reduction ability, it has a high activity for solar hydrogen evolution. Xu et al. developed a metallic 1T-MoS_2/O-g-C_3N_4 heterostructure using the *in situ* growth method which exhibited a relatively greater performance when compared to 2H-MoS_2/O-g-C_3N_4 material [127]. The major reason for the greater performance is the more exposed edge sites, active basal planes, and closed contact layers between the two components. This close contact is more favorable to transfer photogenerated electrons from the conduction band of O-g-C_3N_4 to the surface of 1T-MoS_2, which leads to the greater performance of the 1T-MoS_2/ O-g-C_3N_4 system. Du et al. also reported a novel photocatalyst 1T-MoS_2/CdS hybrid for photocatalytic hydrogen evolution. The optimized hybrid shows 35-folds improvements in photocatalytic hydrogen evolution in visible light radiation when compared to pure CdS nanosheets [128]. Jin et al. reported a unique heterostructure which consists of exfoliated 1T-MoS_2 on planar p-Si and behaves as the efficient and robust photocathode for solar driven HER [129]. This

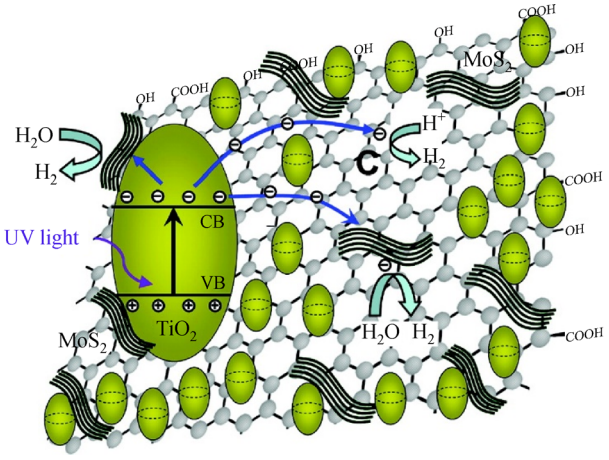

Fig. 12 Schematic illustration of the charge transfer in TiO_2/MG composites (The proposed mechanism for the enhanced electron transfer in the TiO_2/MG system under irradiation assumes that the photo excited electrons are transferred from the CB of TiO_2 not only to the MoS_2 nanosheets but also to the C atoms in the graphene sheets, which can effectively reduce H^+ to produce H_2 (Reproduced from Ref. [131] with permission from American Chemical Society)

unique heterostructure exhibits an excellent onset of photocurrent and a high current density for planar p-Si photocathodes which uses non-noble metal catalyst. From the electrochemical impedance spectroscopy measurements demonstration, it is inferred that the excellent performance of the CVD grown 1T-MoS_2 /p-Si photocathode is due to the smaller charge-transfer resistance across the interfaces of semiconductor and catalyst or catalyst and electrolyte. The electrochemical impedance spectroscopy measurements also showed slow carrier recombination dynamics and efficient charge carrier separation. Another research developed a new novel heterostructure ammoniated with MoS_2 with a unique 1T/2H phase by using the facile hydrothermal approach [130]. The enhancement of the electronic conductivity increase in density of the active sites and improved efficiency in both electro transfer and mass transport are resulted from the presence of the 1T phase in MoS_2. Due to the presence of both the 1T/2H phases of MoS_2, the photo electrocatalytic properties are improved.

Carbon materials play important roles in improving the interfacial charge transfer between MoS_2 catalysts and the electrode substrate. Xiang et al. synthesized a layered MoS_2/graphene hybrid and incorporated it with TiO_2 to form a new composite material [131]. As shown in Fig. 12, under light irradiation, electrons transfer from the valence band of TiO_2 to the conduction band of TiO_2. Subsequently, one part of the electrons is directly delivered to MoS_2, while the other part of the electrons flows to MoS_2 through graphene. The edge sites of MoS_2 can effectively reduce water to H_2. The introduction of graphene material can remarkably improve the charge transport and hinder the recombination of electrons with holes.

5 Conclusions and outlook

As a repressive layered transition metal dichalcogenides (TMDs), MoS_2 has been widely invested for solar energy conversion applications. In this review, the recent progress of MoS_2 for its applications in the fields of solar thermal water purification, photocatalytic process, and photoelectrocatalytic HER has been summarized. In particular, the recent advances of structure control, elemental doping and synthesis methods for preparing MoS_2 have been described. Besides, their potential advantages and limitations have also been emphasized, such as the rapid recombination of photo generated carriers, limited active edge sites and difficulties in photocatalyst recycling that hinder the practical application of MoS_2-based photocatalysts in solar energy conversion. In conclusion, MoS_2 has been experiencing a renaissance in recent years, largely owing to the demand for renewable energy conversion and storage. The unique properties of MoS_2-based photocatalysts and their good performance in different applications suggest that it is a promising earth-abundant photocatalyst. Although experimental results on a laboratory scale have been reported, the real application of MoS_2 as catalytic or electrode materials is still challenging. This means that more encouraging studies are highly desirable in this field.

References

1. Wang Q H, Kalantar-Zadeh K, Kis A, Coleman J N, Strano M S. Electronics and optoelectronics of two-dimensional transition metal dichalcogenides. Nature Nanotechnology, 2012, 7(11): 699–712

2. Geim A K, Novoselov K S. The rise of graphene. Nature Materials, 2007, 6(3): 183–191
3. Rao C N R, Maitra U, Matte H S S R. Synthesis, characterization, and selected properties of graphene. In: Rao C N, Sood A K, eds. Graphene: Synthesis, Properties, and Phenomena. Wiley, 2013, 1–47
4. Huang X, Qi X, Boey F, Zhang H. Graphene-based composites. Chemical Society Reviews, 2012, 41(2): 666–686
5. Huang X, Yin Z, Wu S, Qi X, He Q, Zhang Q, Yan Q, Boey F, Zhang H. Graphene-based materials: synthesis, characterization, properties, and applications. Small, 2011, 7(14): 1876–1902
6. Huang X, Zeng Z, Zhang H. Metal dichalcogenide nanosheets: preparation, properties and applications. Chemical Society Reviews, 2013, 42(5): 1934–1946
7. Chhowalla M, Shin H S, Eda G, Li L J, Loh K P, Zhang H. The chemistry of two-dimensional layered transition metal dichalcogenide nanosheets. Nature Chemistry, 2013, 5(4): 263–275
8. Wilson J A, Yoffe A. The transition metal dichalcogenides discussion and interpretation of the observed optical, electrical and structural properties. Advances in Physics, 1969, 18(73): 193–335
9. Ataca C, Sahin H, Ciraci S. Stable, single-layer MX_2 transition-metal oxides and dichalcogenides in a honeycomb-like structure. Journal of Physical Chemistry C, 2012, 116(16): 8983–8999
10. Chhowalla M, Shin H S, Eda G, Li L J, Loh K P, Zhang H. The chemistry of two-dimensional layered transition metal dichalcogenide nanosheets. Nature Chemistry, 2013, 5(4): 263–275
11. Rao C N R, Maitra U, Waghmare U V. Extraordinary attributes of 2-dimensional MoS_2 nanosheets. Chemical Physics Letters, 2014, 609: 172–183
12. Tan C, Zhang H. Two-dimensional transition metal dichalcogenide nanosheet-based composites. Chemical Society Reviews, 2015, 44 (9): 2713–2731
13. Huang X, Tan C, Yin Z, Zhang H. 25th Anniversary Article: Hybrid nanostructures based on two-dimensional nanomaterials. Advanced Materials, 2014, 26(14): 2185–2204
14. Novoselov K, Jiang D, Schedin F, Booth T J, Khotkevich V V, Morozov S V, Geim A K. Two-dimensional atomic crystals. Proceedings of the National Academy of Sciences of the United States of America, 2005, 102(30): 10451–10453
15. Singh E, Nalwa HS. Graphene-based bulk-heterojunction solar cells: a review. Journal of Nanoscience and Nanotechnology, 2015, 15(9): 6237–6278
16. Singh E, Nalwa H S. Stability of graphene-based heterojunction solar cells. RSC Advances, 2015, 5(90): 73575–73600
17. Geim A K, Grigorieva I V. Van der Waals heterostructures. Nature, 2013, 499(7459): 419–425
18. Cao X, Tan C, Zhang X, Zhao W, Zhang H. Solution-processed two-dimensional metal dichalcogenide-based nanomaterials for energy storage and conversion. Advanced Materials, 2016, 28(29): 6167–6196
19. Chia X, Ambrosi A, Sofer Z, Luxa J, Pumera M. Catalytic and charge transfer properties of transition metal dichalcogenides arising from electrochemical pretreatment. ACS Nano, 2015, 9(5): 5164–5179
20. Chou S S, Sai N, Lu P, Coker E N, Liu S, Artyushkova K, Luk T S, Kaehr B, Brinker C J. Understanding catalysis in a multiphasic two-dimensional transition metal dichalcogenide. Nature Communications, 2015, 6(1): 8311
21. Loo A H, Bonanni A, Sofer Z, Pumera M. Transitional metal/chalcogen dependant interactions of hairpin DNA with transition metal dichalcogenides, MX_2. ChemPhysChem, 2015, 16(11): 2304–2306
22. Kalantar-zadeh K, Ou J Z, Daeneke T, Strano M S, Pumera M, Gras S L. Two-dimensional transition metal dichalcogenides in biosystems. Advanced Functional Materials, 2015, 25(32): 5086–5099
23. Sarkar D, Xie X, Kang J, Zhang H, Liu W, Navarrete J, Moskovits M, Banerjee K. Functionalization of transition metal dichalcogenides with metallic nanoparticles: implications for doping and gas-sensing. Nano Letters, 2015, 15(5): 2852–2862
24. Kertesz M, Hoffmann R. Octahedral vs. trigonal-prismatic coordination and clustering in transition-metal dichalcogenides. Journal of the American Chemical Society, 1984, 106(12): 3453–3460
25. Divigalpitiya W R, Morrison S R, Frindt R. Thin oriented films of molybdenum disulphide. Thin Solid Films, 1990, 186(1): 177–192
26. Voiry D, Salehi M, Silva R, Fujita T, Chen M, Asefa T, Shenoy V B, Eda G, Chhowalla M. Conducting MoS_2 nanosheets as catalysts for hydrogen evolution reaction. Nano Letters, 2013, 13(12): 6222–6227
27. Li Y, Wang H, Xie L, Liang Y, Hong G, Dai H. MoS_2 nanoparticles grown on graphene: an advanced catalyst for the hydrogen evolution reaction. Journal of the American Chemical Society, 2011, 133(19): 7296–7299
28. Toh R J, Sofer Z, Luxa J, Sedmidubský D, Pumera M. 3R phase of MoS_2 and WS_2 outperforms the corresponding 2H phase for hydrogen evolution. Chemical Communications, 2017, 53(21): 3054–3057
29. Ambrosi A, Sofer Z, Pumera M. $2H \rightarrow 1T$ phase transition and hydrogen evolution activity of MoS_2, $MoSe_2$, WS_2 and WSe_2 strongly depends on the MX_2 composition. Chemical Communications, 2015, 51(40): 8450–8453
30. Novoselov K S, Jiang D, Schedin F, Booth T J, Khotkevich V V, Morozov S V, Geim A K. Two-dimensional atomic crystals. Proceedings of the National Academy of Sciences of the United States of America, 2005, 102(30): 10451–10453
31. Yin Z, Li H, Li H, Jiang L, Shi Y, Sun Y, Lu G, Zhang Q, Chen X, Zhang H. Single-layer MoS_2 phototransistors. ACS Nano, 2012, 6 (1): 74–80
32. Li H, Lu G, Yin Z, He Q, Li H, Zhang Q, Zhang H. Optical identification of single- and few-layer MoS_2 sheets. Small, 2012, 8 (5): 682–686
33. Li H, Lu G, Wang Y, Yin Z, Cong C, He Q, Wang L, Ding F, Yu T, Zhang H. Mechanical exfoliation and characterization of single- and few-layer nanosheets of WSe_2, TaS_2, and $TaSe_2$. Small, 2013, 9(11): 1974–1981
34. Li H, Yin Z, He Q, Li H, Huang X, Lu G, Fam D W H, Tok A I Y, Zhang Q, Zhang H. Fabrication of single- and multilayer MoS_2 film-based field-effect transistors for sensing NO at room

temperature. Small, 2012, 8(1): 63–67
35. Zeng Z, Yin Z, Huang X, Li H, He Q, Lu G, Boey F, Zhang H. Single-layer semiconducting nanosheets: high-yield preparation and device fabrication. Angewandte Chemie International Edition, 2011, 50(47): 11093–11097
36. Zeng Z, Sun T, Zhu J, Huang X, Yin Z, Lu G, Fan Z, Yan Q, Hng H H, Zhang H. An effective method for the fabrication of few-layer-thick Inorganic nanosheets. Angewandte Chemie International Edition, 2012, 51(36): 9052–9056
37. Coleman J N, Lotya M, O'Neill A, Bergin S D, King P J, Khan U, Young K, Gaucher A, De S, Smith R J, Shvets I V, Arora S K, Stanton G, Kim H Y, Lee K, Kim G T, Duesberg G S, Hallam T, Boland J J, Wang J J, Donegan J F, Grunlan J C, Moriarty G, Shmeliov A, Nicholls R J, Perkins J M, Grieveson E M, Theuwissen K, McComb D W, Nellist P D, Nicolosi V. Two-dimensional nanosheets produced by liquid exfoliation of layered materials. Science, 2011, 331(6017): 568–571
38. Zhou K G, Mao N N, Wang H X, Peng Y, Zhang H L. A mixed-solvent strategy for efficient exfoliation of inorganic graphene analogues. Angewandte Chemie International Edition, 2011, 50 (46): 10839–10842
39. Shi Y, Zhou W, Lu A Y, Fang W, Lee Y H, Hsu A L, Kim S M, Kim K K, Yang H Y, Li L J, Idrobo J C, Kong J. van der Waals epitaxy of MoS_2 layers using graphene as growth templates. Nano Letters, 2012, 12(6): 2784–2791
40. Liu K K, Zhang W, Lee Y H, Lin Y C, Chang M T, Su C Y, Chang C S, Li H, Shi Y, Zhang H, Lai C S, Li L J. Growth of large-area and highly crystalline MoS_2 thin layers on insulating substrates. Nano Letters, 2012, 12(3): 1538–1544
41. Radisavljevic B, Radenovic A, Brivio J, Giacometti V, Kis A. Single-layer MoS_2 transistors. Nature Nanotechnology, 2011, 6(3): 147–150
42. Splendiani A, Sun L, Zhang Y, Li T, Kim J, Chim C Y, Galli G, Wang F. Emerging photoluminescence in monolayer MoS_2. Nano Letters, 2010, 10(4): 1271–1275
43. Lee K, Kim H Y, Lotya M, Coleman J N, Kim G T, Duesberg G S. Electrical characteristics of molybdenum disulfide flakes produced by liquid exfoliation. Advanced Materials, 2011, 23(36): 4178–4182
44. Eda G, Yamaguchi H, Voiry D, Fujita T, Chen M, Chhowalla M. Photoluminescence from chemically exfoliated MoS_2. Nano Letters, 2011, 11(12): 5111–5116
45. Voiry D, Goswami A, Kappera R, Silva C C C, Kaplan D, Fujita T, Chen M, Asefa T, Chhowalla M. Covalent functionalization of monolayered transition metal dichalcogenides by phase engineering. Nature Chemistry, 2015, 7(1): 45–49
46. Py M, Haering R. Structural destabilization induced by lithium intercalation in MoS_2 and related compounds. Canadian Journal of Physics, 1983, 61(1): 76–84
47. Heising J, Kanatzidis M G. Structure of restacked MoS_2 and WS_2 elucidated by electron crystallography. Journal of the American Chemical Society, 1999, 121(4): 638–643
48. Eda G, Fujita T, Yamaguchi H, Voiry D, Chen M, Chhowalla M. Coherent atomic and electronic heterostructures of single-layer MoS_2. ACS Nano, 2012, 6(8): 7311–7317
49. Voiry D, Goswami A, Kappera R, Silva C C C, Kaplan D, Fujita T, Chen M, Asefa T, Chhowalla M. Covalent functionalization of monolayered transition metal dichalcogenides by phase engineering. Nature Chemistry, 2015, 7(1): 45–49
50. Lee Y H, Zhang X Q, Zhang W, Chang M T, Lin C T, Chang K D, Yu Y C, Wang J T W, Chang C S, Li L J, Lin T W. Synthesis of large-area MoS_2 atomic layers with chemical vapor deposition. Advanced Materials, 2012, 24(17): 2320–2325
51. Zhan Y, Liu Z, Najmaei S, Ajayan P M, Lou J. Large-area vapor-phase growth and characterization of MoS_2 atomic layers on a SiO_2 substrate. Small, 2012, 8(7): 966–971
52. Lin Y C, Zhang W, Huang J K, Liu K K, Lee Y H, Liang C T, Chu C W, Li L J. Wafer-scale MoS_2 thin layers prepared by MoO_3 sulfurization. Nanoscale, 2012, 4(20): 6637–6641
53. Xie X, Ao Z, Su D, Zhang J, Wang G. MoS_2/Graphene composite anodes with enhanced performance for sodium-Ion batteries: the role of the two-dimensional heterointerface. Advanced Functional Materials, 2015, 25(9): 1393–1403
54. Shi Z T, Kang W, Xu J, Sun Y W, Jiang M, Ng T W, Xue H T, Yu D Y W, Zhang W, Lee C S. Hierarchical nanotubes assembled from MoS_2-carbon monolayer sandwiched superstructure nanosheets for high-performance sodium ion batteries. Nano Energy, 2016, 22: 27–37
55. Wang M, Li G, Xu H, Qian Y, Yang J. Enhanced lithium storage performances of hierarchical hollow MoS_2 nanoparticles assembled from nanosheets. ACS Applied Materials & Interfaces, 2013, 5(3): 1003–1008
56. Xie J, Zhang H, Li S, Wang R, Sun X, Zhou M, Zhou J, Lou X W D, Xie Y. Defect-rich MoS_2 ultrathin nanosheets with additional active edge sites for enhanced electrocatalytic hydrogen evolution. Advanced Materials, 2013, 25(40): 5807–5813
57. Ramakrishna Matte H S S, Gomathi A, Manna A K, Late D J, Datta R, Pati S K, Rao C N R. MoS_2 and WS_2 analogues of graphene. Angewandte Chemie International Edition, 2010, 49(24): 4059–4062
58. Lu Y, Yao X, Yin J, Peng G, Cui P, Xu X. MoS_2 nanoflowers consisting of nanosheets with a controllable interlayer distance as high-performance lithium ion battery anodes. RSC Advances, 2015, 5(11): 7938–7943
59. Wang P P, Sun H, Ji Y, Li W, Wang X. Three-dimensional assembly of single-layered MoS_2. Advanced Materials, 2014, 26 (6): 964–969
60. Wang Z, Mi B. Environmental applications of 2D molybdenum disulfide (MoS_2) nanosheets. Environmental Science & Technology, 2017, 51(15): 8229–8244
61. Scalise E, Houssa M, Pourtois G, Afanas′ev V V, Stesmans A. First-principles study of strained 2D MoS_2. Physica E, Low-Dimensional Systems and Nanostructures, 2014, 56: 416–421
62. Mak K F, Lee C, Hone J, Shan J, Heinz T F. Atomically thin MoS_2: a new direct-gap semiconductor. Physical Review Letters, 2010, 105(13): 136805
63. Han S, Kwon H, Kim S K, Ryu S, Yun W S, Kim D H, Hwang J H, Kang J S, Baik J, Shin H J, Hong S C. Band-gap transition induced by interlayer van der Waals interaction in MoS_2. Physical Review. B, 2011, 84(4): 045409

64. Ebnonnasir A, Narayanan B, Kodambaka S, Ciobanu C V. Tunable MoS_2 band gap in MoS_2-graphene heterostructures. Applied Physics Letters, 2014, 105(3): 031603
65. Peelaers H, Van de Walle C G. Effects of strain on band structure and effective masses in MoS_2. Physical Review. B, 2012, 86(24): 241401
66. Lipatov A, Sharma P, Gruverman A, Sinitskii A. Optoelectrical molybdenum disulfide (MoS_2) ferroelectric memories. ACS Nano, 2015, 9(8): 8089–8098
67. Cheiwchanchamnangij T, Lambrecht W R. Quasiparticle band structure calculation of monolayer, bilayer, and bulk MoS_2. Physical Review. B, 2012, 85(20): 205302
68. Shi H, Pan H, Zhang Y W, Yakobson B I. Quasiparticle band structures and optical properties of strained monolayer MoS_2 and WS_2. Physical Review. B, 2013, 87(15): 155304
69. Tongay S, Zhou J, Ataca C, Lo K, Matthews T S, Li J, Grossman J C, Wu J. Thermally driven crossover from indirect toward direct bandgap in 2D semiconductors: $MoSe_2$ versus MoS_2. Nano Letters, 2012, 12(11): 5576–5580
70. Scheer R, Schock H W. Chalcogenide Photovoltaics: Physics, Technologies, and Thin Film Devices. John Wiley & Sons, 2011
71. Smith A M, Nie S. Semiconductor nanocrystals: structure, properties, and band gap engineering. Accounts of Chemical Research, 2010, 43(2): 190–200
72. Zhang H, Zhou W, Yang Z, Wu S, Ouyang F, Xu H. A first-principles study of impurity effects on monolayer MoS_2: bandgap dominated by donor impurities. Materials Research Express, 2017, 4(12): 126301
73. Kim S, Fisher B, Eisler H J, Bawendi M. Type-II quantum dots: CdTe/CdSe (core/shell) and CdSe/ZnTe (core/shell) heterostructures. Journal of the American Chemical Society, 2003, 125(38): 11466–11467
74. Zhao W, Liu Y, Wei Z, Yang S, He H, Sun C. Fabrication of a novel p–n heterojunction photocatalyst n-$BiVO_4$@ p-MoS_2 with core–shell structure and its excellent visible-light photocatalytic reduction and oxidation activities. Applied Catalysis B: Environmental, 2016, 185: 242–252
75. Li H, Yu K, Lei X, Guo B, Fu H, Zhu Z. Hydrothermal synthesis of novel MoS_2/$BiVO_4$ hetero-nanoflowers with enhanced photocatalytic activity and a mechanism investigation. Journal of Physical Chemistry C, 2015, 119(39): 22681–22689
76. Meng F, Li J, Cushing S K, Zhi M, Wu N. Solar hydrogen generation by nanoscale p–n junction of p-type molybdenum disulfide/n-type nitrogen-doped reduced graphene oxide. Journal of the American Chemical Society, 2013, 135(28): 10286–10289
77. Ji K, Deng J, Zang H, Han J, Arandiyan H, Dai H. Fabrication and high photocatalytic performance of noble metal nanoparticles supported on 3DOM $InVO_4$–$BiVO_4$ for the visible-light-driven degradation of rhodamine B and methylene blue. Applied Catalysis B: Environmental, 2015, 165: 285–295
78. Ho W, Yu J C, Lin J, Yu J, Li P. Preparation and photocatalytic behavior of MoS_2 and WS_2 nanocluster sensitized TiO_2. Langmuir, 2004, 20(14): 5865–5869
79. Zong X, Yan H, Wu G, Ma G, Wen F, Wang L, Li C. Enhancement of photocatalytic H_2 evolution on CdS by loading MoS_2 as cocatalyst under visible light irradiation. Journal of the American Chemical Society, 2008, 130(23): 7176–7177
80. Xu H, Li H, Wu C, Chu J, Yan Y, Shu H, Gu Z. Preparation, characterization and photocatalytic properties of Cu-loaded $BiVO_4$. Journal of Hazardous Materials, 2008, 153(1–2): 877–884
81. Kang J, Sahin H, Peeters F O M. Tuning carrier confinement in the MoS_2/WS_2 lateral heterostructure. Journal of Physical Chemistry C, 2015, 119(17): 9580–9586
82. Lahiri J, Lin Y, Bozkurt P, Oleynik I I, Batzill M. An extended defect in graphene as a metallic wire. Nature Nanotechnology, 2010, 5(5): 326–329
83. Zou X, Liu Y, Yakobson B I. Predicting dislocations and grain boundaries in two-dimensional metal-disulfides from the first principles. Nano Letters, 2013, 13(1): 253–258
84. Singh A K, Yakobson B I. Electronics and magnetism of patterned graphene nanoroads. Nano Letters, 2009, 9(4): 1540–1543
85. Hu Z, Zhang S, Zhang Y N, Wang D, Zeng H, Liu L M. Modulating the phase transition between metallic and semiconducting single-layer MoS_2 and WS_2 through size effects. Physical Chemistry Chemical Physics, 2015, 17(2): 1099–1105
86. Kang J, Li J, Li S S, Xia J B, Wang L W. Electronic structural Moiré pattern effects on MoS_2/$MoSe_2$ 2D heterostructures. Nano Letters, 2013, 13(11): 5485–5490
87. Zhang L, Drummond E, Brodney M A, Cianfrogna J, Drozda S E, Grimwood S, Vanase-Frawley M A, Villalobos A. Design, synthesis and evaluation of [3H]PF-7191, a highly specific nociceptin opioid peptide (NOP) receptor radiotracer for in vivo receptor occupancy (RO) studies. Bioorganic & Medicinal Chemistry Letters, 2014, 24(22): 5219–5223
88. Ghim D, Jiang Q, Cao S, Singamaneni S, Jun Y S. Mechanically interlocked 1T/2H phases of MoS_2 nanosheets for solar thermal water purification. Nano Energy, 2018, 53: 949–957
89. Hoffmann M R, Martin S T, Choi W, Bahnemann D W. Environmental applications of semiconductor photocatalysis. Chemical Reviews, 1995, 95(1): 69–96
90. Fujishima A, Honda K. Electrochemical photolysis of water at a semiconductor electrode. Nature, 1972, 238(5358): 37–38
91. Ding Q, Song B, Xu P, Jin S. Efficient electrocatalytic and photoelectrochemical hydrogen generation using MoS_2 and related compounds. Chem, 2016, 1(5): 699–726
92. Wang Q H, Kalantar-Zadeh K, Kis A, Coleman J N, Strano M S. Electronics and optoelectronics of two-dimensional transition metal dichalcogenides. Nature Nanotechnology, 2012, 7(11): 699–712
93. Karunadasa H I, Montalvo E, Sun Y, Majda M, Long J R, Chang C J. A molecular MoS_2 edge site mimic for catalytic hydrogen generation. Science, 2012, 335(6069): 698–702
94. Chang K, Li M, Wang T, Ouyang S, Li P, Liu L, Ye J. Drastic layer-number-dependent activity enhancement in photocatalytic H_2 evolution over $n$$MoS_2$/CdS ($n \geqslant 1$) under visible light. Advanced Energy Materials, 2015, 5(10): 1402279
95. Han H, Kim K M, Lee C W, Lee C S, Pawar R C, Jones J L, Hong Y R, Ryu J H, Song T, Kang S H, Choi H, Mhin S. Few-layered metallic 1T-MoS_2/TiO_2 with exposed (001) facets: two-dimensional nanocomposites for enhanced photocatalytic activities.

Physical Chemistry Chemical Physics, 2017, 19(41): 28207–28215

96. Hsiao M C, Chang C Y, Niu L J, Bai F, Li L J, Shen H H, Lin J Y, Lin T W. Ultrathin 1T-phase MoS_2 nanosheets decorated hollow carbon microspheres as highly efficient catalysts for solar energy harvesting and storage. Journal of Power Sources, 2017, 345: 156–164
97. Hu C, Zheng S, Lian C, Chen F, Lu T, Hu Q, Duo S, Zhang R, Guan C. α-S nanoparticles grown on MoS_2 nanosheets: a novel sulfur-based photocatalyst with enhanced photocatalytic performance. Journal of Molecular Catalysis A Chemical, 2015, 396: 128–135
98. Ding Y, Zhou Y, Nie W, Chen P. MoS_2–GO nanocomposites synthesized via a hydrothermal hydrogel method for solar light photocatalytic degradation of methylene blue. Applied Surface Science, 2015, 357: 1606–1612
99. Zhang W, Xiao X, Zheng L, Wan C. Fabrication of TiO_2/MoS_2@ zeolite photocatalyst and its photocatalytic activity for degradation of methyl orange under visible light. Applied Surface Science, 2015, 358: 468–478
100. Zhu C, Zhang L, Jiang B, Zheng J, Hu P, Li S, Wu M, Wu W. Fabrication of Z-scheme Ag_3PO_4/MoS_2 composites with enhanced photocatalytic activity and stability for organic pollutant degradation. Applied Surface Science, 2016, 377: 99–108
101. Kumar S, Baruah A, Tonda S, Kumar B, Shanker V, Sreedhar B. Cost-effective and eco-friendly synthesis of novel and stable N-doped ZnO/gC_3N_4 core-shell nanoplates with excellent visible-light responsive photocatalysis. Nanoscale, 2014, 6(9): 4830–4842
102. Theerthagiri J, Senthil R, Malathi A, Selvi A, Madhavan J, Ashokkumar M. Synthesis and characterization of a CuS–WO_3 composite photocatalyst for enhanced visible light photocatalytic activity. RSC Advances, 2015, 5(65): 52718–52725
103. Zhang L, Sun L, Liu S, Huang Y, Xu K, Ma F. Effective charge separation and enhanced photocatalytic activity by the heterointerface in MoS_2/reduced graphene oxide composites. RSC Advances, 2016, 6(65): 60318–60326
104. Jo W K, Adinaveen T, Vijaya J J, Sagaya Selvam N C. Synthesis of MoS_2 nanosheet supported Z-scheme TiO_2/gC_3N_4 photocatalysts for the enhanced photocatalytic degradation of organic water pollutants. RSC Advances, 2016, 6(13): 10487–10497
105. Kumar S, Sharma V, Bhattacharyya K, Krishnan V. Synergetic effect of MoS_2–RGO doping to enhance the photocatalytic performance of ZnO nanoparticles. New Journal of Chemistry, 2016, 40(6): 5185–5197
106. Xia J, Ge Y, Zhao D, Di J, Ji M, Yin S, Li H, Chen R. Microwave-assisted synthesis of few-layered MoS_2/BiOBr hollow microspheres with superior visible-light-response photocatalytic activity for ciprofloxacin removal. CrystEngComm, 2015, 17(19): 3645–3651
107. Wang C, Lin H, Xu Z, Cheng H, Zhang C. One-step hydrothermal synthesis of flowerlike MoS_2/CdS heterostructures for enhanced visible-light photocatalytic activities. RSC Advances, 2015, 5(20): 15621–15626
108. Gamage J, Zhang Z. Applications of photocatalytic disinfection. International Journal of Photoenergy, 2010, 764870
109. Agnihotri S, Bajaj G, Mukherji S, Mukherji S. Arginine-assisted immobilization of silver nanoparticles on ZnO nanorods: an enhanced and reusable antibacterial substrate without human cell cytotoxicity. Nanoscale, 2015, 7(16): 7415–7429
110. Hajipour M J, Fromm K M, Akbar Ashkarran A, Jimenez de Aberasturi D, Larramendi I R, Rojo T, Serpooshan V, Parak W J, Mahmoudi M. Antibacterial properties of nanoparticles. Trends in Biotechnology, 2012, 30(10): 499–511
111. Sunada K, Watanabe T, Hashimoto K. Studies on photokilling of bacteria on TiO_2 thin film. Journal of Photochemistry and Photobiology A Chemistry, 2003, 156: 227–233
112. Sirelkhatim A, Mahmud S, Seeni A, Kaus N H M, Ann L C, Bakhori S K M, Hasan H, Mohamad D. Review on zinc oxide nanoparticles: antibacterial activity and toxicity mechanism. Nano-Micro Letters, 2015, 7(3): 219–242
113. Awasthi G P, Adhikari S P, Ko S, Kim H J, Park C H, Kim C S. Facile synthesis of ZnO flowers modified graphene like MoS_2 sheets for enhanced visible-light-driven photocatalytic activity and antibacterial properties. Journal of Alloys and Compounds, 2016, 682: 208–215
114. Liu W, Feng Y, Tang H, Yuan H, He S, Miao S. Immobilization of silver nanocrystals on carbon nanotubes using ultra-thin molybdenum sulfide sacrificial layers for antibacterial photocatalysis in visible light. Carbon, 2016, 96: 303–310
115. Liu Y R, Hu W H, Li X, Dong B, Shang X, Han G Q, Chai Y M, Liu Y Q, Liu C G. Facile one-pot synthesis of CoS_2-MoS_2/CNTs as efficient electrocatalyst for hydrogen evolution reaction. Applied Surface Science, 2016, 384: 51–57
116. Wen M Q, Xiong T, Zang Z G, Wei W, Tang X S, Dong F. Synthesis of MoS_2/g-C_3N_4 nanocomposites with enhanced visible-light photocatalytic activity for the removal of nitric oxide (NO). Optics Express, 2016, 24(10): 10205–10212
117. Yuan Y J, Tu J R, Ye Z J, Chen D Q, Hu B, Huang Y W, Chen T T, Cao D P, Yu Z T, Zou Z G. MoS_2-graphene/$ZnIn_2S_4$ hierarchical microarchitectures with an electron transport bridge between light-harvesting semiconductor and cocatalyst: a highly efficient photocatalyst for solar hydrogen generation. Applied Catalysis B: Environmental, 2016, 188: 13–22
118. Powers D E, Hansen S G, Geusic M E, Puiu A C, Hopkins J B, Dietz T G, Duncan M A, Langridge-Smith P R R, Smalley R E. Supersonic metal cluster beams: laser photoionization studies of copper cluster (Cu_2). Journal of Physical Chemistry, 1982, 86(14): 2556–2560
119. Chen X, Shen S, Guo L, Mao S S. Semiconductor-based photocatalytic hydrogen generation. Chemical Reviews, 2010, 110(11): 6503–6570
120. Xu Y, Schoonen M A A. The absolute energy positions of conduction and valence bands of selected semiconducting minerals. American Mineralogist, 2000, 85(3–4): 543–556
121. Laursen A B, Kegnæs S, Dahl S, Chorkendorff I. Molybdenum sulfides—efficient and viable materials for electro- and photoelectrocatalytic hydrogen evolution. Energy & Environmental Science, 2012, 5(2): 5577–5591
122. Yuan Y J, Yu Z T, Li Y H, Lu H W, Chen X, Tu W G, Ji Z G, Zou Z

G. A MoS_2/6,13-pentacenequinone composite catalyst for visible-light-induced hydrogen evolution in water. Applied Catalysis B: Environmental, 2016, 181: 16–23

123. Yuan Y J, Ye Z J, Lu H W, Hu B, Li Y H, Chen D Q, Zhong J S, Yu Z T, Zou Z G. Constructing anatase TiO_2 nanosheets with exposed (001) facets/layered MoS_2 two-dimensional nanojunctions for enhanced solar hydrogen generation. ACS Catalysis, 2016, 6(2): 532–541
124. Liu Y R, Hu W H, Li X, Dong B, Shang X, Han G Q, Chai Y M, Liu Y Q, Liu C G. One-pot synthesis of hierarchical Ni_2P/MoS_2 hybrid electrocatalysts with enhanced activity for hydrogen evolution reaction. Applied Surface Science, 2016, 383: 276–282
125. He H Y. Efficient hydrogen evolution activity of 1T-MoS_2/Si-doped TiO_2 nanotube hybrids. International Journal of Hydrogen Energy, 2017, 42(32): 20739–20748
126. Li X B, Gao Y J, Wu H L, Wang Y, Guo Q, Huang M Y, Chen B, Tung C H, Wu L Z. Assembling metallic 1T-MoS_2 nanosheets with inorganic-ligand stabilized quantum dots for exceptional solar hydrogen evolution. Chemical Communications, 2017, 53(41): 5606–5609
127. Xu H, Yi J, She X, Liu Q, Song L, Chen S, Yang Y, Song Y, Vajtai R, Lou J, Li H, Yuan S, Wu J, Ajayan P M. 2D heterostructure comprised of metallic 1T-MoS_2/Monolayer O-g-C_3N_4 towards efficient photocatalytic hydrogen evolution. Applied Catalysis B: Environmental, 2018, 220: 379–385
128. Du P, Zhu Y, Zhang J, Xu D, Peng W, Zhang G, Zhang F, Fan X. Metallic 1T phase MoS_2 nanosheets as a highly efficient co-catalyst for the photocatalytic hydrogen evolution of CdS nanorods. RSC Advances, 2016, 6(78): 74394–74399
129. Ding Q, Meng F, English C R, Cabán-Acevedo M, Shearer M J, Liang D, Daniel A S, Hamers R J, Jin S. Efficient photoelectrochemical hydrogen generation using heterostructures of Si and chemically exfoliated metallic MoS_2. Journal of the American Chemical Society, 2014, 136(24): 8504–8507
130. Wang D, Su B, Jiang Y, Li L, Ng B K, Wu Z, Liu F. Polytype 1T/2H MoS_2 heterostructures for efficient photoelectrocatalytic hydrogen evolution. Chemical Engineering Journal, 2017, 330: 102–108
131. Xiang Q, Yu J, Jaroniec M. Synergetic effect of MoS_2 and graphene as cocatalysts for enhanced photocatalytic H_2 production activity of TiO_2nanoparticles. Journal of the American Chemical Society, 2012, 134(15): 6575–6578
132. Chou S S, Kaehr B, Kim J, Foley B M, De M, Hopkins P E, Huang J, Brinker C J, Dravid V P. Chemically exfoliated MoS_2 as near-infrared photothermal agents. Angewandte Chemie, 2013, 125 (15): 4254–4258